Ultra-Slow Coarsening in Precipitation-Strengthened Refractory High-Entropy Alloys

R.J. Vikram[1], Sandipan Sen[1], Liu Yang[1], Michael K. Eusterholz[1,2], Amin Radi[1], Daniel Schliephake[1,2], Jean-Philippe Couzinié[3], Alexander Kauffmann[4], Martin Heilmaier[1]

[1]Institute for Applied Materials (IAM-WK), Karlsruhe Institute of Technology (KIT), Engelbert-Arnold-Str. 4, 76131 Karlsruhe, Germany
[2]Karlsruhe Nano Micro Facility (KNMFi), Karlsruhe Institute of Technology (KIT), Hermann-von-Helmholtz-Platz 1, 76344 Eggenstein-Leopoldshafen, Germany
[3]Université Paris Est, ICMPE (UMR 7182), CNRS, UPEC, 2-8, Rue H. Dunant, F-94320, Thiais, France
[4]Institute for Materials (IM), Ruhr University Bochum (RUB), Universitätsstr. 150, 44780 Bochum, Germany

* corresponding authors' mail addresses:
raja.vikram@partner.kit.edu (R.J. Vikram), sandipan.sen@kit.edu (S. Sen)
alexander.kauffmann@rub.de (A. Kauffmann), martin.heilmaier@kit.edu (M. Heilmaier)

Abstract

The mechanical behavior of precipitation-strengthened materials is strongly influenced by precipitate shape, size, volume fraction, and lattice misfit to the matrix they are embedded in. This study examines the impact of adding 1 at.% Zr on thermal stability and coarsening kinetics in a refractory high-entropy alloy with the composition 27.3Ta-27.3Mo-27.3Ti-8Cr-10Al (at.%) consisting of a disordered A2 matrix and ordered B2 precipitates. We demonstrate that this minor Zr addition does not lead to the formation of other intermetallic phases and induces a pronounced change in the precipitate morphology from cuboidal/elongated to spherical, accompanied by an increased number density. Atom probe tomography reveals a strong Zr partitioning to the precipitates resulting in extremely slow coarsening kinetics when compared to other alloy classes. Overall, this work underscores the potential of tailoring precipitate characteristics to potentially enhance microstructural stability of B2 precipitates and, consequently, creep resistance in advanced body-centered superalloys.

Keywords: Refractory high entropy alloys, B2 precipitates, Coarsening, Ripening.

1. Introduction

The advancement of high-temperature structural (metallic) materials, most notably superalloys, depends on the precise control of matrix-precipitate misfit and precipitate morphology [1–5]. Alloying elements play a crucial role in tailoring these microstructural features, which in turn significantly influence the mechanical properties, particularly the creep resistance [6,7]. Spherical precipitates are often reported to result in good thermal stability and slow coarsening kinetics due to only a small lattice mismatch contributing to elastic strain energy [8–10].

Research on Ni- and Co-based superalloys showed that the matrix-precipitates lattice misfit can be tuned by alloying, affecting precipitate morphology. In Ni-based alloys (with A1-$L1_2$ two-phase microstructure $(\gamma - \gamma')$, Al, Ti, Ta, and Nb favor the formation of coherent $L1_2$, while Re and W enhance solid solution strengthening of the A1 matrix [11]. In emerging BCC superalloys, including Cr-, W- or Fe-based systems, elements like Al, Ti, and Ta are often used to form strengthening B2 or $L2_1$ precipitates [12–16].

While the change in lattice misfit and precipitate morphology with micro-alloying is well documented in A1-$L1_2$ systems [17], similar studies in A2-B2 refractory high entropy alloys (RHEA) are missing. Recently, 27.3Ta-27.3Mo-27.3Ti-8Cr-10Al (at.%, TMT-8Cr-10Al) was reported exhibiting an A2–B2 microstructure. Its B2 phase is stable up to ≈1060 °C and forms by a nucleation and growth mechanism. It has a slight positive relative difference of lattice parameters δ of (+ 0.6 ± 0.4) % (constraint condition) [18]. This relative difference in lattice parameters is expressed by:

$$\delta = \frac{2(a_{B2} - a_{A2})}{a_{B2} + a_{A2}} \quad (1)$$

where a_{A2} and a_{B2} represent the lattice parameters of A2 and B2, respectively. It is worth mentioning that a critical misfit (unconstrained condition) of $\delta \approx 0.4$ % has been identified in Ni-based superalloys above which misfit strain significantly influences the $L1_2$ precipitate coarsening kinetics and microstructural evolution [19].

Studies on Cr-based superalloys (A2–B2 microstructure; $\delta \approx 0.1$ %) have demonstrated lower coarsening rates (10^2 nm³/h at 1000 °C) than those observed in Fe-, Co-, and Ni-based superalloys. The coarsening kinetics suggest low A2/B2 interfacial energies of around 40 mJ/m² at 1000 °C and are primarily attributed to the limited solubility of Ni and Al in the Cr matrix [6].

Thermal stability in TMT-8Cr-10Al might be further improved if δ is reduced closer to zero, an outcome achievable through microalloying. The B2 precipitates were found to be rich in Al and Ti, while the A2 matrix was enriched in Mo and Ta with Cr being equally distributed in both phases. Studies on $Al_{0.5}NbTa_{0.8}Ti_{1.5}V_{0.2}Zr$ [20] have revealed the presence of a B2-ordered phase primarily composed of Ti, Al, and Zr. However, the A2–B2 microstructure in this alloy is thermally unstable due to the formation of ω phase precipitates during prolonged annealing [21]. Given that the B2 phase in the TMT-8Cr-10Al is also rich in Ti and Al, 1 at.% Zr was chosen as alloying addition to target the B2 phase. Thus, the final composition of the new alloy investigated in this study is 27Ta-27Mo-27Ti-8Cr-10Al-1Zr (TMT-8Cr-10Al-1Zr).

2. Materials and Methods

Both alloys (TMT-8Cr-10Al and TMT-8Cr-10Al-1Zr) were synthesized using an Edmund Bühler GmbH AM/0.5 arc melting furnace under an Ar atmosphere. High-purity elements (Ta, Cr, Al and Zr 99.9 %, Mo 99.95 %, Ti 99.8 %) were sourced from chemPUR GmbH, Germany. 100 g buttons were produced as described elsewhere [18,22]. To investigate the microstructure, samples were cut from the buttons using electrical discharge machining (EDM). A standard metallographic procedure was applied [18,22] and scanning electron microscopy (SEM) was performed using a Zeiss LEO 1530 (Zeiss, Germany) operated at an acceleration voltage of 20 kV. Electron backscatter diffraction (SEM-EBSD) analysis was carried out using an EDAX Digiview system (Ametek, USA) integrated into a Zeiss Auriga 60 (Zeiss, Germany) to examine local crystallographic orientations and identify secondary phases. Differential scanning calorimetry (DSC) measurements were carried out for TMT-8Cr-10Al-1Zr to investigate the heat signatures of the ordering and precipitation reactions and to compare them to TMT-8Cr-10Al. Details are provided

in [18,22,23]. CALPHAD calculations using Pandat software (CompuTherm LLC) with the RHEA database were employed to determine solidus temperatures using the nominal alloy compositions. These allow for the determination of a homologous temperature $T_{\mathrm{hom}} = T/T_{\mathrm{solidus}}$ across different alloys.

To evaluate thermal stability and aging kinetics, homogenized specimens underwent solution heat treatment at 1200 °C for 1 h followed by rapid water quenching. These samples were then subjected to isothermal aging at 1000 °C for durations reaching 1000 h to systematically study microstructural evolution over extended timeframes. The samples were wrapped in a Ta foil and sealed in Ar-filled fused silica tubes to prevent oxidation.

Quantitative image analysis was conducted using ImageJ [24] on high-resolution SEM micrographs to evaluate the morphology and distribution of the B2 phase. The procedures for image segmentation and the parameters used for analyzing precipitate distribution [25] are provided in the supplementary file.

Atom probe tomography (APT) samples were prepared in a Strata 400 focus ion beam/scanning electron microscopy dual-beam device (Thermo Fisher Scientific, Waltham, MA, USA) using the lift-out method [26]. APT analysis was performed with a LEAP 4000X HR instrument (Cameca Instruments, Madison, WI, USA) at 50 K, at a detection rate of 0.5 %, and with a laser wavelength of 355 nm with a pulse energy of 40 pJ and pulse rate of 125 kHz. The APT reconstruction and data evaluation was performed with AP Suite 6.3 (Cameca Instruments).

To assess the aspect of brittleness or plastic deformability in the A2–B2 multiphase alloy system, microindentation tests were conducted using a Qness Q10+ microhardness tester under loads of HV1–HV5 to generate intense localized plastic deformation regions.

3. Results and Discussion

The XRD pattern of TMT-8Cr-10Al-1Zr (supplementary material) suggests only A2 or B2 crystal structure being present. Microstructural investigations of Zr-free TMT-8Cr-10Al quenched after long-term annealing revealed the diffusion-controlled phase separation between 1060 to 1070 °C [18]. The ordering reaction at 1055 °C was furthermore investigated by the extrapolation of peak temperatures in DSC measurements to 0 K/min. The temperature dependence of the enthalpy derivative dH/dT of TMT-8Cr-10Al-1Zr for different heating rates is shown in **Figure 1a**. The extrapolated peak temperature is 1056 °C and thus very close to the report on the Zr-free alloy [22]. Inverse pole figure (IPF) mapping from SEM-EBSD shows equiaxed grains with a size exceeding 200 µm in diameter and random crystallographic orientations (**Figure 1b**). The homogenized microstructure of the alloy is represented in **Figure 1c**. High-magnification backscattered electron (SEM-BSE) micrographs reveal fine B2 precipitates dispersed throughout the A2 matrix (**Figure 1d**). As the microstructural appearance and thermal behavior of TMT-8Cr-10Al and TMT-8Cr-10Al-1Zr are very similar, no significant changes in the phase stabilities are concluded.

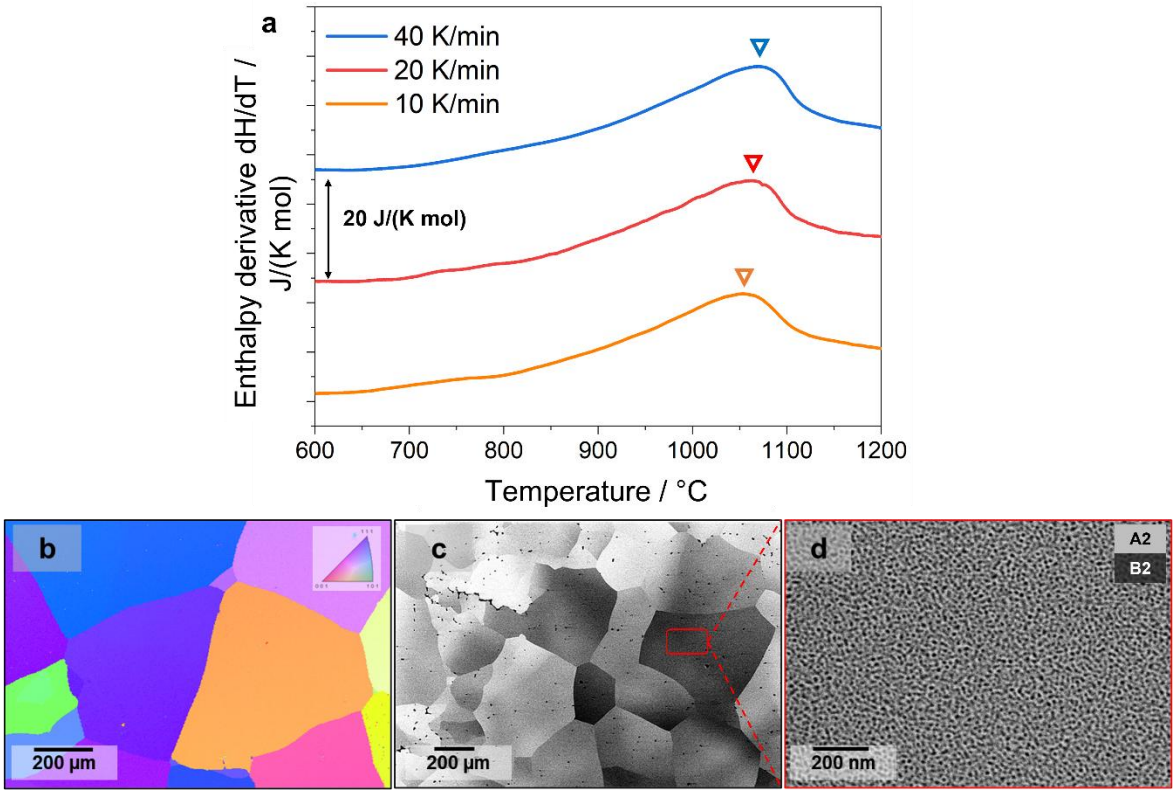

Figure 1. Characterization of homogenized **TMT-8Cr-10Al-1Zr**: (a) DSC results with varying heating rates, (b) SEM-EBSD IPF map revealing equiaxed grains with random crystallographic texture. SEM-BSE mode at increasing magnifications, illustrating the homogenized microstructure: (c) low magnification overview (orientation contrast) showing grains with sizes exceeding 200 µm, (d) high magnification detail (Z contrast) highlighting evenly distributed spherical B2 precipitates.

A coarsening study was conducted at 1000 °C for durations of 10, 100, and 1000 h for both alloys. As illustrated in **Figure 2a-f**, the TMT-8Cr-10Al-1Zr retains spherical precipitates with minimal coarsening over time (**Figure 2d-f**). By contrast, the TMT-8Cr-10Al undergoes directional coarsening leading to elongated precipitates due to its positive δ between the precipitate and matrix [1,18]. The spherical precipitate shape strongly suggests a near zero δ [27]. This morphological stability is likely to enhance the high-temperature mechanical properties, particularly the creep resistance [28,29].

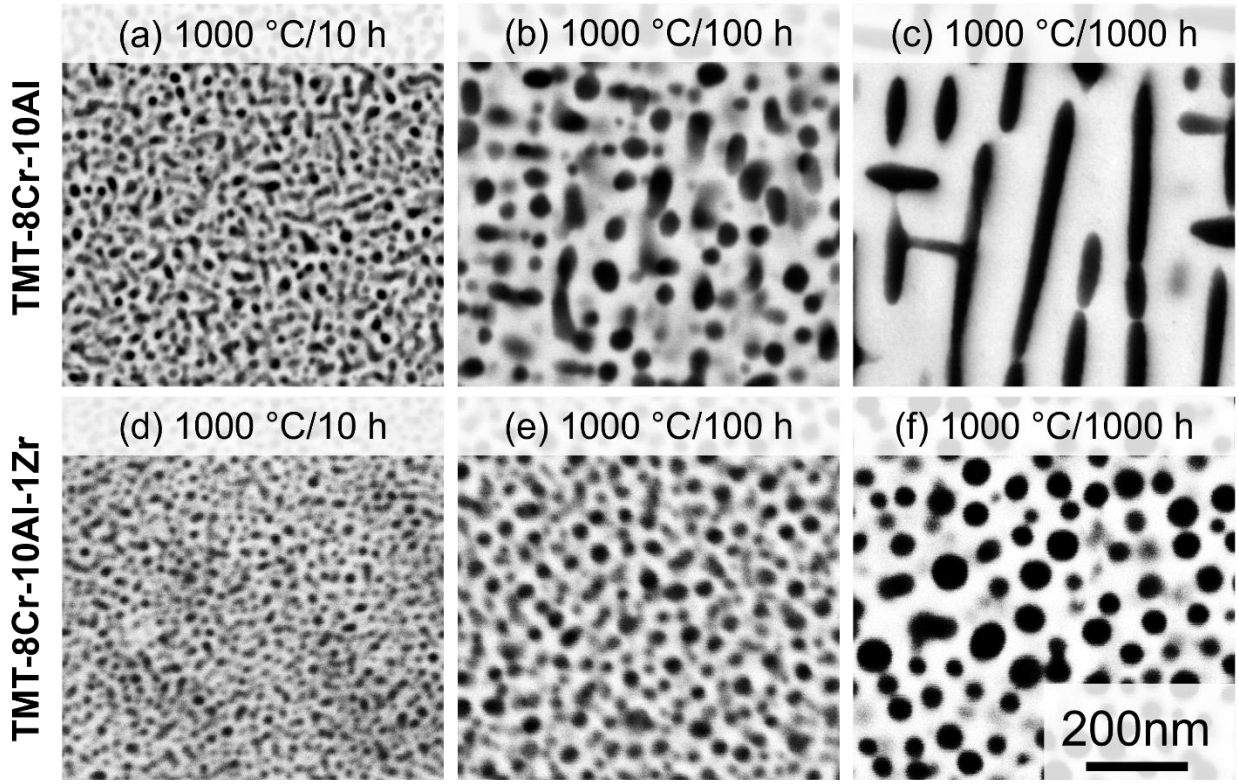

Figure 2. Evolution of microstructure in (a-c) **TMT-8Cr-10Al**, and (d-f) and **TMT-8Cr-10Al-1Zr**, both aged at 1000 °C for 10, 100 and 1000 h. SEM-BSE micrographs (Z contrast) illustrating the distribution and morphology of B2 precipitates in the A2 matrix. Note the distinct differences in precipitate shape and size distribution between the Zr-free and Zr-containing alloys across different ageing durations.

Table 1. Comparative analysis of microstructural features in TMT-8Cr-10Al and TMT-8Cr-10Al-1Zr at 1000 ˚C.

Parameters	**TMT-8Cr-10Al**				**TMT-8Cr-10Al-1Zr**			
Time / h	**10**	**100**	**200**	**1000**	**10**	**100**	**200**	**1000**
Actual mean diameter / nm	31 ± 14	46 ± 19	52 ± 36	86 ± 22	17 ± 7	35 ± 12	48 ± 18	72 ± 31
area% B2	29 ± 2	29 ± 1	26 ± 2	26 ± 3	29 ± 3	29 ± 2	27 ± 2	28 ± 1
Mean Center-to-center particle spacing L / nm	40 ± 3	62 ± 3	75 ± 5	122 ± 7	25 ± 2	48 ± 4	65 ± 3	107 ± 4
Circularity index	0.63 ± 0.21	0.71 ± 0.15	0.60 ± 0.12	0.49 ± 0.20	0.68 ± 0.18	0.85 ± 0.13	0.84 ± 0.11	0.82 ± 0.12
Number density N_V / 10^3 μm^3	58	19	9.4	3.6	310	40	14	4.1

Table 1 shows the coarsening kinetics revealing distinct differences between the alloys. Zr-free TMT-8Cr-10Al exhibits systematically larger equivalent diameters across all aging durations, paired with a slightly lower precipitate area fraction after 1000 h at 1000 °C. After 10 h aging, TMT-8Cr-10Al-1Zr showed an order-of-magnitude higher precipitate number density demonstrating enhanced nucleation. The evolution of circularity confirms the visual observation of shape stability in TMT-8Cr-10Al-1Zr. Zr addition reduces δ and internal stresses as the primary driver of directional coarsening. Thereby, coarsening is decelerated as well [30,31].

APT analysis on TMT-8Cr-10Al-1Zr aged at 1000 °C for 100 h was performed to investigate the partitioning behavior between matrix and precipitates. The Ta isosurfaces in the 3D reconstruction in **Figure 3a** reveal the B2 precipitates. 1D-concentration profiles were generated across an A2/B2 interface to quantify the elemental distribution, **Figure 3b**. These profiles indicate a strong Zr partitioning into the B2 phase. **Figure 3c** shows a magnified region highlighting Al, Cr and Zr concentration profiles from **Figure 3b**. Like for TMT-8Cr-10Al [22,23], the B2 precipitates in TMT-8Cr-10Al-1Zr are also enriched in Ti and Al in addition to Zr. The A2 matrix is likewise enriched in Ta and Mo while being depleted in Zr. Cr is uniformly distributed. **Table 2** presents the chemical composition of the elements in the two phases (in at.%) for both alloys. The Ti/Al and Ti/Mo ratios approach 2 suggesting that the B2 phase resembles Ti_2AlMo [32,33].

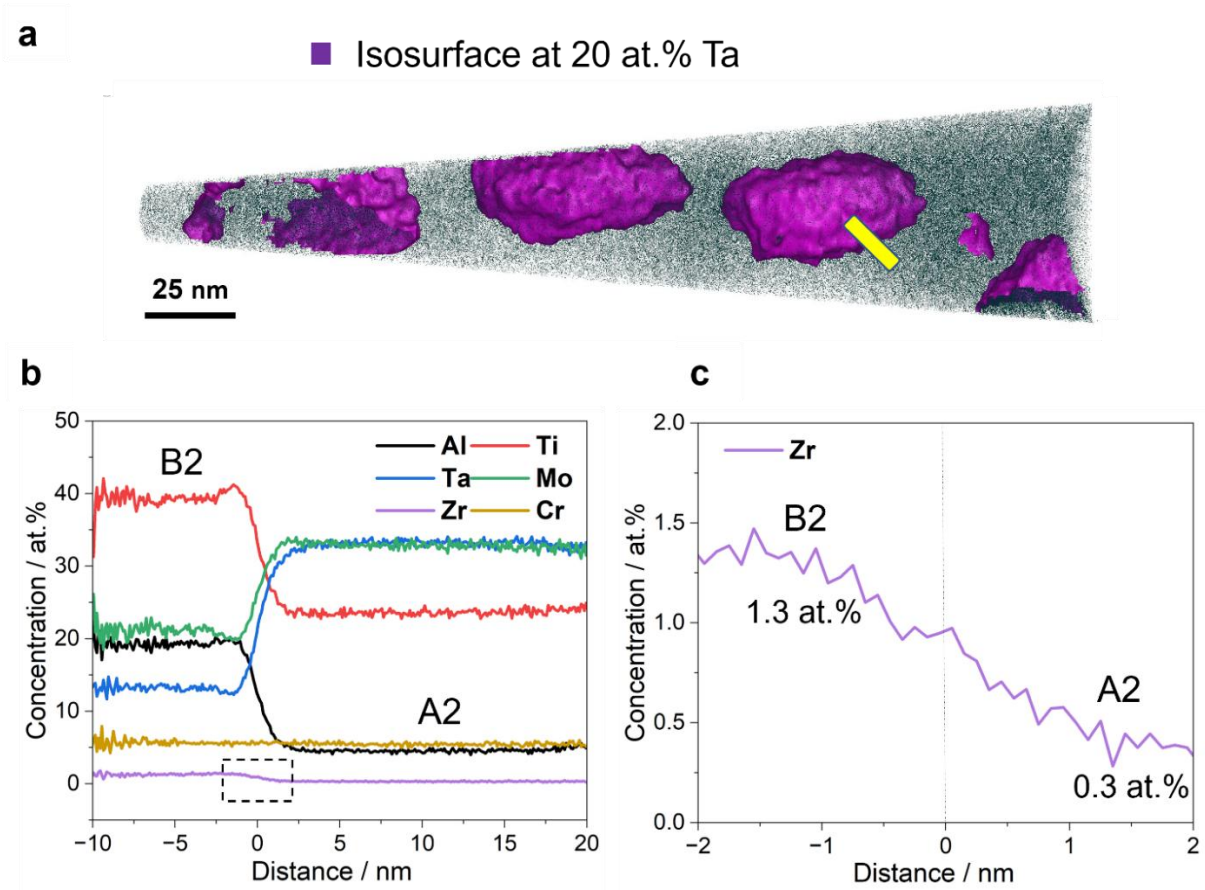

Figure 3. APT analysis of the A2–B2 microstructure in TMT-8Cr-10Al-1Zr. (a) 3D reconstruction showing Ta isosurface (pink) in the analyzed volume. (b) Proximity histograms across the A2/B2 interface for the two central precipitates shown in (a) and (c) magnified concentration profile highlighting Zr concentration at the A2/B2 interface.

The coarsening behavior and morphology of the precipitates are determined by the interplay between minimizing the misfit strain energy and interfacial energy [34,35]. The spherical precipitate morphology in TMT-8Cr-10Al-1Zr indicates the dominance of interfacial energy over misfit strain energy [36,37]. Although the morphology of the precipitates remains quite stable, the coarsening rates are important to quantify by using:

$$\bar{r}_{\mathrm{act}}^{n} - \bar{r}_{0}^{n} = \kappa\, t \tag{2}$$

$\bar{r}_0$ is the radius after completion of the precipitation reaction, $\bar{r}_{\mathrm{act}}$ the mean precipitate radius after different aging times t and κ the coarsening rate constant. The power-law exponent n is time-independent, if the coarsening mechanism remains unchanged. $n = 3$ is obtained for bulk diffusion-controlled coarsening [38]. Based on the Lifshitz-Slyozov-Wagner theory [39], κ can be approximated in a multicomponent system as [38,40]:

$$\kappa = \frac{8\gamma\, V_{\mathrm{m}}^{\mathrm{B2}}\, D_i^{\mathrm{A2}}}{9R\,T\sum_i^N \left(c_i^{\mathrm{B2}} - c_i^{\mathrm{A2}}\right)^2 / c_i^{\mathrm{A2}}} \tag{3}$$

γ is the interfacial energy, $V_{\mathrm{m}}^{\mathrm{B2}}$ the molar volume of B2 precipitate, R the gas constant, T the absolute temperature, c_i^j and D_i^j the concentration and diffusion coefficient of i in phase j [33].

Figure 4a shows the variation of $\bar{r}_{\mathrm{act}}^3$ with respect to t. The κ for TMT-8Cr-10Al-1Zr is very small with (48 ± 4) nm^3/h at 1000 °C. Such a low κ is highlighted when compared to TMT-8Cr-10Al, newly developed Ni-based (A1–L1$_2$) and Cr-based superalloys (A2–B2) in **Figure 4b**. It can be clearly inferred that TMT-8Cr-10Al-1Zr exhibits slower coarsening kinetics at much higher T/T_{solvus} as compared to other superalloys.

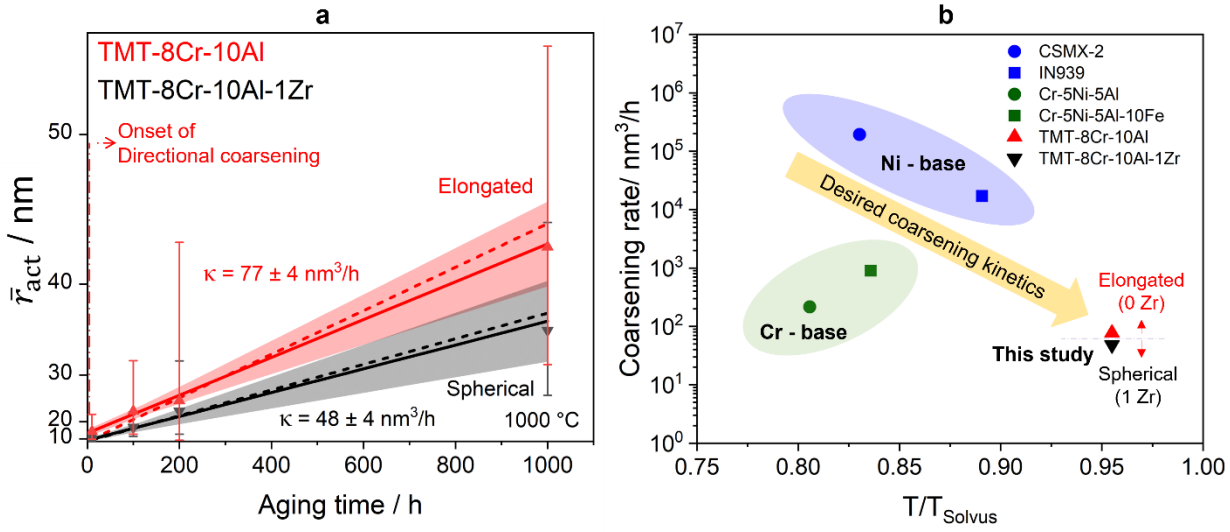

Figure 4. (a) Plot of $\bar{r}_{\mathrm{act}}^3$ vs. ageing time for determining the coarsening rate. $\bar{r}_{\mathrm{act}}$ is used for clarity and physical interpretation; fitting parameters and the role of r_{o} are detailed in the Supplementary Information. (b) Coarsening rate as a function of ageing temperature for ferritic, Ni-, and Cr-based superalloys [6], normalized to their respective precipitate solvus temperatures T_{solvus}.

κ is influenced by four key factors: the interfacial energy γ, molar volume V_{m}, diffusivity D of the constituent species, and the concentration gradient $\Delta C_{\mathrm{i}} = \left(c_i^{\mathrm{B2}} - c_i^{\mathrm{A2}}\right)^2 / c_i^{\mathrm{A2}}$ of the constituent species between the matrix and precipitates. κ is directly proportional to γ, V_{m} and D while being inversely proportional to the squared relative concentration difference ΔC_{i}.

When comparing the coarsening behavior of TMT-8Cr-10Al and TMT-8Cr-10Al-1Zr, the similarities in composition suggest that D and V_{m} are likely comparable. The concentration gradient ΔC_i in TMT-8Cr-10Al and TMT-8Cr-10Al-1Zr is relatively small for Ta, Mo and Ti, but more significant for Al, see **Table 2**. However, in complex multicomponent alloys, it is generally accepted that the coarsening kinetics—specifically the evolution of average radius and number density—are primarily controlled by the species with lowest diffusivity [41,42]. Since the difference in ΔC_i for Ta and Mo is minor in both alloys, their contributions to κ are expected to be similar. Consequently, any difference in κ between these two alloys is likely attributed to variations in the interfacial energy γ. The latter typically comprises a chemical contribution γ_{ch} and an elastic strain contribution γ_{el} [43]. The elastic component γ_{el} is directly proportional to the square of the lattice misfit δ^2. For TMT-8Cr-10Al, δ is approximately +0.6 % (in constraint condition), whereas it is close to 0 for TMT-8Cr-10Al-1Zr. As a result, γ_{el} and the total interfacial energy γ is expected to be higher in TMT-8Cr-10Al. This higher γ (factor of 1.5) leads to a higher κ (factor of 1.5), consistent with experimental observations.

When comparing κ across different alloy systems, the analysis becomes more complex. In this discussion, we consider two A2–B2 alloy systems, TMT-8Cr-10Al/-1Zr (*Ta-Mo-Ti alloys*) and Cr-5Ni-5Al/Cr-5Ni-5Al-10Fe (*Cr-Ni-Al alloys*). For both systems, the lattice misfit can be assumed to be comparable due to the presence of stable spherical precipitates, suggesting a similar contribution of the interfacial energy γ to κ. However, the other three parameters influencing κ, namely V_{m}, D, and ΔC_i likely differ significantly. Based on data from **Table 2**, ΔC_i is higher in the Cr-Ni-Al alloys than in Ta-Mo-Ti alloys. Additionally, due to the presence of elements with larger atomic radii such as Ta and Mo, V_{m} of the B2 precipitates in the Ta-Mo-Ti alloys is expected to be larger than in the Cr-Ni-Al alloys. This combination of a higher V_{m} and lower ΔC_i in the Ta-Mo-Ti alloys would suggest higher κ for this system. However, experimental measurements at 1000 °C indicate the opposite. This discrepancy is most likely attributed to the diffusivity D as the rate-determining factor. While accurate determination of diffusivities in such multicomponent A2–B2 systems is challenging, a qualitative understanding can be obtained by considering the diffusivities of the constituent elements at 1000 °C.

From thermodynamical calculations, T_{solidus} was determined to be 2210 °C for the TMT-8Cr-10Al alloy while T_{solidus} is 1710 °C for the Cr-5Ni-5Al. Thus, the homologous temperatures T_{hom} at 1000 °C are 0.51 and 0.64 for TMT-8Cr-10Al and Cr-5Ni-5Al, respectively. These findings indicate that the diffusivities of the constituent elements may be much faster in the Cr-Ni-Al alloys, which rationalizes the larger κ in the Ta-Mo-Ti alloys. This is in line with experimental reports showing that the diffusivity of Zr in other BCC refractory high entropy alloys increased by two orders of magnitude when the homologous temperature is raised from 0.51 to 0.64 [44]. This simple qualitative analysis leads to conclude that the diffusivity in the A2–B2 alloys is the rate-determining factor for κ over the other parameters. The comparison of the BCC and FCC superalloy systems is of engineering interest. However, a detailed assessment of the individual parameters is not meaningful due to even more assumptions being required.

Table 2 Composition of A2 (matrix) and B2 (precipitate) phases analyzed via APT in the current TMT-8Cr-10Al(+1Zr) alloy and reference A2–B2/A1–$L1_2$ systems, measured at 900–1000 °C for κ parameter analysis. Data highlight important contributing parameter influencing kinetic coarsening behavior.

	Ta-Mo-Ti - Base	Phase	Composition (at.%) Ta	Mo	Ti	Cr	Al	Zr	T / °C	κ / nm^3/h
BCC	TMT-8Cr-10Al-1Zr	**A2**	32.9 ± 0.3	33.3 ± 0.2	23.5 ± 0	5.4 ± 0.1	4.5 ± 0	0.3 ± 0	**1000**	**48 ± 4**
		B2	13.1 ± 0.2	21.1 ± 0.3	39.5 ± 0	5.7 ± 0.3	19.2 ± 0.2	1.3 ± 0.1		
		ΔC_i	**12**	**5**	**12**	**0**	**48**	**3**		
	TMT-8Cr-10Al	**A2**	30.4 ± 0.3	31.5 ± 0.2	25.0 ± 0	7.0 ± 0.1	5.7 ± 0	–	**1000**	**77 ± 4**
		B2	14.8 ± 0.2	21.7 ± 0.3	38.4 ± 0	6.6 ± 0.3	18.2 ± 0.2	–		
		ΔC_i	**8**	**3**	**7**	**0**	**27**	**–**		
	Cr - Base	**Phase**	**Composition (at.%) Cr**	**Ni**	**Al**	**Fe**				
	Cr-5Ni-5Al	**A2**	98.7 ± 0.1	0.3 ± 0.1	0.9 ± 0.1	–			**1000**	**222** [6]
		B2	0.9 ± 0.3	52.7 ± 0.5	46.4 ± 0.5	–				
		ΔC_i	**96**	**9152**	**2300**	**–**				
	Cr-5Ni-5Al-10Fe	**A2**	86.1 ± 0.3	1.2 ± 0.1	1.4	11.2 ± 0.3			**1000**	**914** [6]
		B2	0.9 ± 0.2	51.2 ± 0.3	44.1 ± 0.2	3.7 ± 0.1				
		ΔC_i	**84**	**2083**	**1302**	**5**				
	Ni - Base	**Phase**	**Nominal composition (at.%) Ni,Co**	**Al,Ti**	**Ta,Cr**	**Mo,W**				
FCC	CMSX2	**A1–$L1_2$ (at.%)**	66.4, 4.6	5.6, 1.0	6.0, 7.8	0.6, 7.9			**1000**	**216000** [45]
	IN939	**A1–$L1_2$ (at.%)**	46.2, 18.4	4.1, 4.3	0.4, 24.3	0, 0.6			**910**	**17642** [46]

The resembled Ti_2AlMo type B2 phase is known to exhibit ductility during room temperature deformation [47,48]. The ductility has been attributed to the possible activation of <111>{112} and <111>{011} slip systems owing to its relatively low antiphase boundary (APB) energy [47,49]. The combination with the extremely small size of the precipitates and a low δ might allow for slip transfer through the B2 phase [50]. HV1 Vickers indentation was performed on TMT-8Cr-10Al-1Zr aged at 1000 °C for 1000 h (**Figure 5a**). In regions of intense plastic localization, slip traces were observed. Near the indentation, interaction with B2 precipitates resulted in complete precipitate cutting (**Figure 5b**) [40–42]. Interestingly, the observed behavior suggests that these coherent spherical precipitates have the potential to offer ductility in refractory A2+B2 superalloys at ambient temperature [43,44]. The ability of dislocations to penetrate and transmit through the precipitates confirms their coherency even after prolonged high-temperature aging [49,50]. A similar approach applied to TMT-8Cr-10Al (**Figure 5c,d**)

shows that the elongated precipitates also undergo shearing, suggesting the coherent nature of the B2 precipitate even at a larger misfit. While shape often influences the dislocations-precipitate interaction, the observation that both elongated and spherical precipitate cutting suggests that the critical resolved shear stress required for cutting may be relatively low.

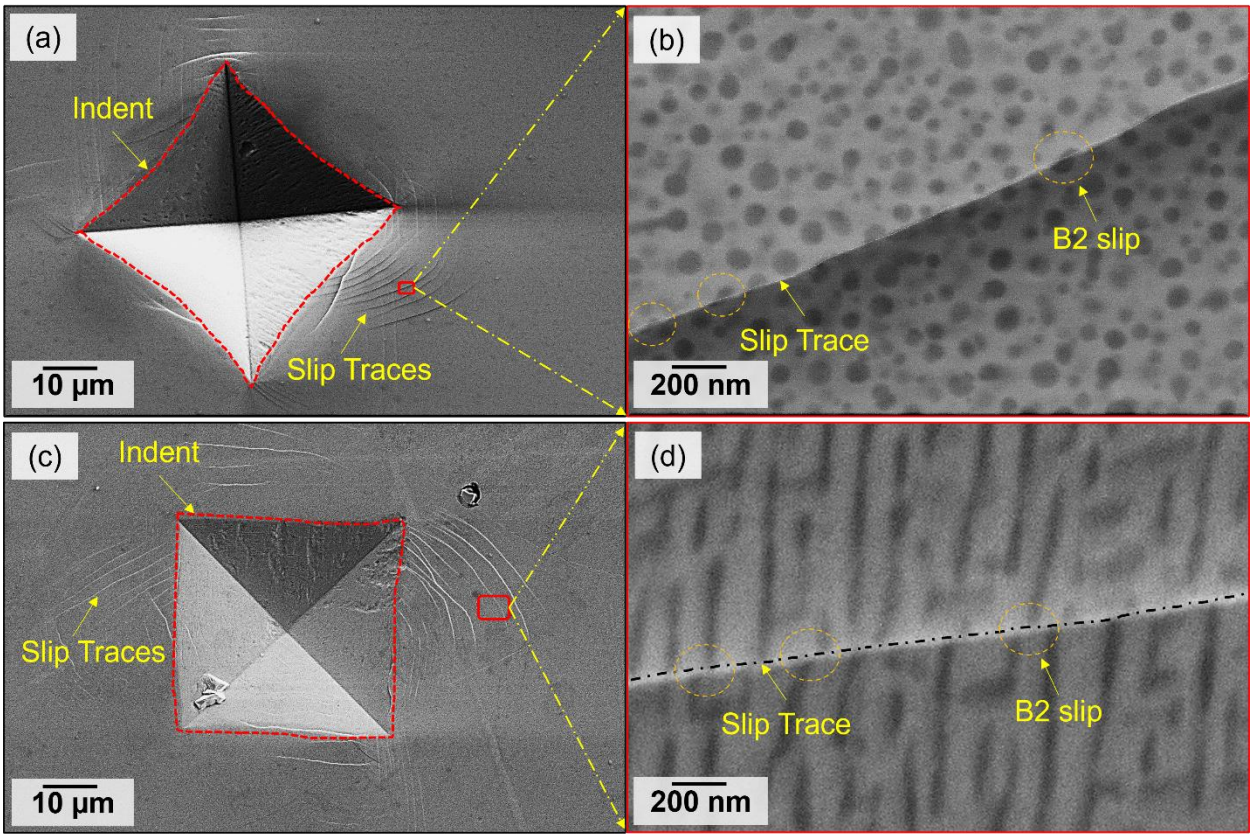

Figure 5. Deformation characteristics of B2 precipitates in A2 matrix in a Zr-containing specimen aged at 1000 °C for 1000 h. Vickers indentation (HV1 load) showing intense localized plastic deformation with prominent slip traces for (a) TMT-8Cr-10A and (c) TMT-8Cr-10Al. High-magnification SE micrographs revealing B2 nanoprecipitates (encircled) cut along the slip direction for (b) TMT-8Cr-10A and (d) TMT-8Cr-10Al. The complete cutting mechanism confirms coherent interfacial matching between B2 precipitates and A2 matrix.

4. Conclusions

The refractory high entropy alloy 27.3Ta-27.3Mo-27.3Ti-8Cr-10Al-1Zr (at.%) with a two-phase, A2 matrix + B2 precipitate microstructure shows promising thermal stability at high temperatures:

1. Microalloying with Zr changes the lattice parameter difference between A2 and B2 to close to zero without forming any undesirable intermetallic phases.
2. Zr is enriched in the spherical, presumably coherent B2 precipitates.
3. The precipitates exhibit exceptional stability against coarsening at 0.98 of their solvus temperature mainly due to slow diffusivity of Ta and Mo.
4. With respect to ductility of A2+B2 alloys, coherency and slip transfer from A2 to B2 is required which is revealed in the investigated alloys.

These findings open a promising avenue for designing advanced BCC superalloys with enhanced mechanical performance.

Acknowledgment

RJV, AK, MH would like to express their sincere gratitude to the Alexander von Humboldt Foundation for their generous funding, which has been pivotal in supporting the research. Their financial assistance enabled us to conduct essential experiments. LY is financially supported by China Scholarship Council (CSC) with No. 202207000023. This work was partly carried out with the support of the Karlsruhe Nano Micro Facility (KNMFi, www.knmf.kit.edu, proposal number 2024-033-032157), a Helmholtz Research Infrastructure at Karlsruhe Institute of Technology (KIT, www.kit.edu).

Data Availability Statement

The data presented in this study are available in KITopen at https://doi.org/10.35097/z3p4z34d6nvynpvq under CC BY-SA 4.0 license. Further information is available upon request with alexander.kauffmann@kit.edu.

Author Contributions

R.J. Vikram: Conceptualization, Methodology, Investigation, Validation, Formal analysis, Data Curation, Visualization, Project administration, Writing - Review & Editing, Writing - Original Draft
Sandipan Sen: Conceptualization, Methodology, Investigation, Formal analysis, Data Curation, Visualization, Writing - Review & Editing
Liu Yang: Methodology, Investigation, Validation, Formal analysis, Data Curation, Visualization, Software, Writing - Review & Editing
Michael Eusterholz: Methodology, Data Curation, Formal analysis, Investigation, Software, Writing - Review & Editing
Amin Radi: Investigation, Writing - Review & Editing
Daniel Schliephake: Investigation, Validation, Formal analysis, Writing – review & editing
Jean-Philippe Couzinié: Investigation, Validation, Formal analysis, Writing – review & editing
Alexander Kauffmann: Conceptualization, Formal analysis, Investigation, Resources, Data Curation, Visualization, Supervision, Writing - Review & Editing
Martin Heilmaier: Conceptualization, Investigation, Supervision, Resources, Investigation, Funding acquisition, Writing- Review & Editing.

Prime novelty statement

We confirm that this manuscript has not been published previously by any of the authors and is not under consideration for publication in another journal.

Declaration of competing interest

The authors declare that they have no known competing financial interests or personal relationships that could have appeared to influence the work reported in this paper.

References

[1] H. Mughrabi, U. Tetzlaff, Microstructure and high-temperature strength of monocrystalline nickel-base superalloys, Adv. Eng. Mat. 2 (2000) 319–326.
[2] J. Zhang, F. Lu, T. Huang, R. Li, G. Zhang, L. Liu, An advanced approach to improve the high-temperature property for Ni-based superalloys: Interface segregation manipulation, Mat Sci Eng A. 881 (2023) 145382.
[3] D.B. Miracle, O.N. Senkov, A critical review of high entropy alloys and related concepts, Acta Mater. 122 (2017) 448–511.

[4] D.B. Miracle, O.N. Senkov, C. Frey, S. Rao, T.M. Pollock, Strength vs temperature for refractory complex concentrated alloys (RCCAs): A critical comparison with refractory BCC elements and dilute alloys, Acta Mater. 266 (2024) 119692.
[5] O.N. Senkov, G.B. Wilks, D.B. Miracle, C.P. Chuang, P.K. Liaw, Refractory high-entropy alloys, Intermet. 18 (2010) 1758–1765.
[6] K. Ma, T. Blackburn, J.P. Magnussen, M. Kerbstadt, P.A. Ferreirós, T. Pinomaa, C. Hofer, D.G. Hopkinson, S.J. Day, P.A.J. Bagot, M.P. Moody, M.C. Galetz, A.J. Knowles, Chromium-based bcc-superalloys strengthened by iron supplements, Acta Mater. 257 (2023) 119183.
[7] N. Parkes, R. Dodds, A. Watson, D. Dye, C. Hardie, S.A. Humphry-Baker, A.J. Knowles, Tungsten-based bcc-superalloys: Thermal stability and ageing behaviour, Int J Refract Met. 113 (2023) 106209.
[8] Y. Ma, B. Jiang, C. Li, Q. Wang, C. Dong, P.K. Liaw, F. Xu, L. Sun, The BCC/B2 morphologies in AlxNiCoFeCr high-entropy alloys, Metals 7 (2017) 57.
[9] T.K. Tsao, A.C. Yeh, C.M. Kuo, K. Kakehi, H. Murakami, J.W. Yeh, S.R. Jian, The High Temperature Tensile and Creep Behaviors of High Entropy Superalloy, Sci Rep. 7 (2017) 12658.
[10] C. Booth-Morrison, R.D. Noebe, D.N. Seidman, effects of a tantalum addition on the morphological and compositional evolution of a model ni-al-cr superalloy, TMS 2008.
[11] Roger C. Reed, The superalloys: fundamentals and applications, Cambridge University Press, 2006.
[12] C. Frey, H. You, S. Kube, G.H. Balbus, K. Mullin, S. Oppenheimer, C.S. Holgate, T.M. Pollock, High Temperature B2 Precipitation in Ru-Containing Refractory Multi-principal Element Alloys, Metall Metall Mater Trans A. 55 (2024) 1739–1764.
[13] M.K. Moczadlo, E.A. Lass, Microstructure and Phase Equilibria in BCC-B2 Nb-Ti-Ru Refractory Superalloys, Mat. 17 (2024) 5429.
[14] Z.T. Kloenne, J.P. Couzinié, M. Heczko, R. Gröger, G.B. Viswanathan, W.A.T. Clark, H.L. Fraser, On the bcc/B2 interface structure in a refractory high entropy alloy, Scr Mater. 223 (2023) 115071.
[15] O.N. Senkov, B. Crossman, S.I. Rao, J.P. Couzinie, D.B. Miracle, T.M. Butler, R. Banerjee, M. Mills, Mechanical properties of an Al10Nb20Ta15Ti30V5Zr20 A2/B2 refractory superalloy and its constituent phases, Acta Mater. 254 (2023) 119017.
[16] A.J. Knowles, D. Dye, R.J. Dodds, A. Watson, C.D. Hardie, S.A. Humphry-Baker, Tungsten-based bcc-superalloys, Appl Mater Today 23 (2021) 101014.
[17] J.S. Van Sluytman, T.M. Pollock, Optimal precipitate shapes in nickel-base γ–γ′ alloys, Acta Mater. 60 (2012) 1771–1783.
[18] L. Yang, S. Sen, D. Schliephake, R.J. Vikram, S. Laube, A. Pramanik, A. Chauhan, S. Neumeier, M. Heilmaier, A. Kauffmann, Creep behavior of a precipitation-strengthened A2-B2 refractory high entropy alloy, Acta Mater. 288 (2025) 120827.
[19] X. Li, N. Saunders, A.P. Miodownik, The coarsening kinetics of γ′ particles in nickel-based alloys, Metall Mater Trans A. 33 (2002) 3367–3373.
[20] J. Brodie, J. Wang, J.-P. Couzinié, M. Heczko, V. Mazánová, M.J. Mills, M. Ghazisaeidi, Stability of the B2 phase in refractory high entropy alloys containing aluminum, Acta Mater. 268 (2024) 119745.
[20] Z.T. Kloenne, K. Kadirvel, J.-P. Couzinie, G.B. Viswanathan, Y. Wang, H.L. Fraser, High temperature phase stability of the compositionally complex alloy AlMo0.5NbTa0.5TiZr, Appl Phys Lett. 119 (2021) 151903.
[21] V. Soni, O.N. Senkov, B. Gwalani, D.B. Miracle, R. Banerjee, Microstructural Design for Improving Ductility of An Initially Brittle Refractory High Entropy Alloy, Sci Rep. 8 (2018) 8816.

[22] S. Laube, S. Schellert, A. Srinivasan Tirunilai, D. Schliephake, B. Gorr, H.J. Christ, A. Kauffmann, M. Heilmaier, Microstructure tailoring of Al-containing compositionally complex alloys by controlling the sequence of precipitation and ordering, Acta Mater. 218 (2021) 117217.
[23] S. Laube, H. Chen, A. Kauffmann, S. Schellert, F. Müller, B. Gorr, J. Müller, B. Butz, H.J. Christ, M. Heilmaier, Controlling crystallographic ordering in Mo–Cr–Ti–Al high entropy alloys to enhance ductility, J Alloys Compd. 823 (2020) 153805.
[24] C.A. Schneider, W.S. Rasband, K.W. Eliceiri, NIH Image to ImageJ: 25 years of image analysis, Nat Met. 9 (2012) 671–675.
[25] R.W. Cahn, P. Haasen, E.J. Kramer, eds., Materials Science and Technology, Wiley, 2007.
[26] D.J. Larson, T.J. Prosa, R.M. Ulfig, B.P. Geiser, T.F. Kelly, Local Electrode Atom Probe Tomography, Springer, New York, 2013.
[27] Y.Y. Zhao, H.W. Chen, Z.P. Lu, T.G. Nieh, Thermal stability and coarsening of coherent particles in a precipitation-hardened (NiCoFeCr)94Ti2Al4 high-entropy alloy, Acta Mater. 147 (2018) 184–194.
[28] G. Song, Z. Sun, L. Li, X. Xu, M. Rawlings, C.H. Liebscher, B. Clausen, J. Poplawsky, D.N. Leonard, S. Huang, Z. Teng, C.T. Liu, M.D. Asta, Y. Gao, D.C. Dunand, G. Ghosh, M. Chen, M.E. Fine, P.K. Liaw, Ferritic Alloys with Extreme Creep Resistance via Coherent Hierarchical Precipitates, Sci Rep. 5 (2015) 16327.
[29] D.G. Morris, M.A. Muñoz-Morris, L.M. Requejo, New iron–aluminium alloy with thermally stable coherent intermetallic nanoprecipitates for enhanced high-temperature creep strength, Acta Mater. 54 (2006) 2335–2341.
[30] J. Li, C. Guo, Y. Ma, Z. Wang, J. Wang, Effect of initial particle size distribution on the dynamics of transient Ostwald ripening: A phase field study, Acta Mater. 90 (2015) 10–26.
[31] B. Zhang, Z.P. Luo, X.Y. Li, Slow precipitate coarsening kinetics in extremely fine nanograined Ni-Cr alloys, Acta Mater. 274 (2024) 119984.
[32] M. Thomas, S. Naka, T. Khan, Stability of the B2 Phase in Ternary Ti–Al–X Alloys (X=Nb, Mo, V), Mat Trans JIM. 35 (1994) 787.
[33] R. Darolia, J. J. Lewandowski, C. T. Liu, P. L. Martin, D. B. Miracle, M. V. Nathal, Structural Intermetallics (conference), Jan 1993.
[34] F. Lu, S. Antonov, S. Lu, J. Zhang, L. Li, D. Wang, J. Zhang, Q. Feng, Unveiling the Re effect on long-term coarsening behaviors of γ′ precipitates in Ni-based single crystal superalloys, Acta Mater. 233 (2022) 117979.
[35] V.A. Vorontsov, J.S. Barnard, K.M. Rahman, H.-Y. Yan, P.A. Midgley, D. Dye, Coarsening behaviour and interfacial structure of γ′ precipitates in Co-Al-W based superalloys, Acta Mater. 120 (2016) 14–23.
[36] S. Kumar, P. Pandey, K. Chattopadhyay, Influence of interfacial and strain energies on γ′ coarsening kinetics in complex concentrated alloys, Mat. 33 (2024) 102018.
[37] S. Laube, A. Kauffmann, S. Schellert, S. Seils, A.S. Tirunilai, C. Greiner, Y.M. Eggeler, B. Gorr, H.-J. Christ, M. Heilmaier, Formation and thermal stability of two-phase microstructures in Al-containing refractory compositionally complex alloys, Sci Technol Adv Mater. 23 (2022) 692–706.
[38] T. Philippe, P.W. Voorhees, Ostwald ripening in multicomponent alloys, Acta Mat. 61 (2013) 4237.
[39] I.M. Lifshitz, V. V Slyozov, the kinetics of precipitation from supersaturated solid solutions, J Phys Chem Sol. 19 (1961) 35.
[40] T. Rieger, J.-M. Joubert, R. Poulain, X. Sauvage, E. Paccou, L. Perrière, I. Guillot, G. Dirras, G. Laplanche, M. Laurent-Brocq, J.-P. Couzinié, Influence of chemical composition on coarsening

kinetics of coherent L12 precipitates in FCC complex concentrated alloys, J Alloys Compd. 967 (2023) 171711.
[41] M. Bonvalet Rolland, A. Borgenstam, Modeling precipitation kinetics in multicomponent alloys during deformation, Front Mater. 9 (2022) 958472.
[42] J.Y.C. Fang, W.H. Liu, T. Yang, Y. Wu, Z.B. Jiao, Multicomponent Precipitation and Strengthening in Intermetallic-Strengthened Alloys, Front Mater. 9 (2022) 931098.
[43] I. Steinbach, Phase-field models in materials science, Model Simul Mat Sci Eng. 17 (2009) 073001.
[44] J. Zhang, C. Gadelmeier, S. Sen, R. Wang, X. Zhang, Y. Zhong, U. Glatzel, B. Grabowski, G. Wilde, S. V. Divinski, Zr diffusion in BCC refractory high entropy alloys: A case of 'non-sluggish' diffusion behavior, Acta Mater. 233 (2022) 117970.
[45] A.M. Ges, O. Fornaro, H.A. Palacio, Coarsening behaviour of a Ni-base superalloy under different heat treatment conditions, Mat Sci and Eng: A. 458 (2007) 96–100.
[46] M.R. Jahangiri, H. Arabi, S.M.A. Boutorabi, Comparison of microstructural stability of IN939 superalloy with two different manufacturing routes during long-time aging, Trans of Nonfer Met Soc of Chi. 24 (2014) 1717–1729.
[47] F. Popille, J. Douin, Comparison of the Deformation Microstructures at Room Temperature in O and B2 Phases of a Ti 2 AlNb Alloy, Le Journal de Physique IV. 06 (1996) C2-211-C2-216.
[48] K. Goyal, C. Bera, N. Sardana, Temperature-dependent structural, mechanical, and thermodynamic properties of B2-phase Ti2AlNb for aerospace applications, J Mater Sci. 57 (2022) 19553–19570.
[49] D. Banerjee, A.K. Gogia, T.K. Nandi, V.A. Joshi, A new ordered orthorhombic phase in a Ti3AlNb alloy, Acta Metal. 36 (1988) 871–882.
[50] G.B. Viswanathan, Z.T. Kloenne, J.P. Couzinié, B.A. Welk, S.J. Kuhr, H.L. Fraser, Deformation mechanisms and their role in the lack of ductility in the refractory-based high entropy alloy AlMo0.5NbTa0.5TiZr, Acta Mater. 269 (2024).